Dopant compensation in alloyed $CH_3NH_3PbBr_{3-x}Cl_x$ perovskite single crystals for gamma-ray spectroscopy

Haotong Wei[1†], Dylan DeSantis[2†], Wei Wei[1], Yehao Deng[1], Dengyang Guo[3], Tom J. Savenije[3], Lei Cao[2] and Jinsong Huang[1,4*]

Organic–inorganic halide perovskites (OIHPs) bring an unprecedented opportunity for radiation detection with their defect-tolerance nature, large mobility–lifetime product, and simple crystal growth from solution. Here we report a dopant compensation in alloyed OIHP single crystals to overcome limitations of device noise and charge collection, enabling γ-ray spectrum collection at room temperature. $CH_3NH_3PbBr_3$ and $CH_3NH_3PbCl_3$ are found to be p-type and n-type doped, respectively, whereas dopant-compensated $CH_3NH_3PbBr_{2.94}Cl_{0.06}$ alloy has over tenfold improved bulk resistivity of $3.6 \times 10^9\ \Omega$ cm. Alloying also increases the hole mobility to $560\ cm^2\ V^{-1}\ s^{-1}$, yielding a high mobility–lifetime product of $1.8 \times 10^{-2}\ cm^2\ V^{-1}$. The use of a guard ring electrode in the detector reduces the crystal surface leakage current and device dark current. A distinguishable ^{137}Cs energy spectrum with comparable or better resolution than standard scintillator detectors is collected under a small electric field of $1.8\ V\ mm^{-1}$ at room temperature.

The strong penetrating capability of high-energy ionizing photons (for example, X-ray or γ-ray) enables the non-invasive detection of condensed objects with radiation detectors that are widely used in many fields including medical imaging, shipping container inspection, radiological and nuclear defence, environmental monitoring, decontamination, homeland security, academic research and so on[1–3]. In addition to radiation dose, the energy spectrum of ionizing photons is another important piece of information that must be known for many applications, such as radioactive species identification. Unlike intensity-mapping-based X-ray radiography, γ-ray energy spectrum detection needs a detector to work in pulse mode, under which the radiation field is typically much weaker than that in current mode, and the detector is performing event-by-event analysis to sort out the intensity versus energy of the radiation quanta. The energy-resolved spectrum is constructed by histogramming the electrical pulse height produced by photons interacting with the detector's material. Therefore, the objective of obtaining a good-resolution energy spectrum imposes strict requirements to radiation detection materials, as well as the sizes of materials in terms of competition with Schubweg distance. Semiconductor radiation detectors for high-energy-photon detection require materials with a large detecting volume to intercept radiation, a large linear attenuation coefficient, large and balanced electron and hole mobility (μ)–charge carrier lifetime (τ) product ($\mu\tau$ product) for efficient charge collection, and finally, high resistivity and low charge trap density to avoid charge trapping under single-event analysis[4]. Among the semiconductors with relatively strong attenuation, high-purity germanium (HPGe) that was developed in the 1970s gives a γ-ray detector the best resolution, which however needs liquid nitrogen cooling due to its small bandgap[5]. Zinc-alloyed CdTe ($Cd_{1-x}Zn_xTe$, denoted CZT for $0 < x < 0.2$) single crystals with a large bandgap of above 1.6 eV possess a high resistivity up to $10^8 \sim 10^9\ \Omega$ cm at room temperature as well as a large $\mu\tau$ product, and thus produce the best resolution γ-ray spectrum among non-cooled semiconductor radiation detectors[6–8]. However, there are many limitations for the application of CZT detectors, such as the cost-restricted crystal manufacturing at a scaled up level, the incompatibility of high-temperature crystal growth with read-out circuits, and low hole mobilities[7,8]. The slow development progress of the CZT γ-ray detector is heavily limited by the material development.

Organic–inorganic halide perovskites (OIHPs), which have made significant successes in the applications of solar cells[9,10], light-emitting diodes[11] and photodetectors[12], are showing a great promise as a new generation of radiation detection materials[13–17]. In addition to their large $\mu\tau$ product, these materials in a single-crystal form have a low charge trap density and defect-tolerant nature, making them particularly attractive for radiation detection[15,16,18]. High-quality perovskite single crystals can be grown from a solution at room temperature with low-cost raw materials[15,16,19]. The high atomic number (Z) of Pb, I and Br as well as the relatively large material density of about $4.0\ g\ cm^{-3}$ enables respectable attenuation of high-energy photons[13,14,16]. We reported the large $\mu\tau$ product of methylammonium lead triiodide ($MAPbI_3$) single crystal and its application in gamma-ray energy harvesting with a 4% efficiency operated in a gammavoltaic mode[15]. Later the $CH_3NH_3PbBr_3$ single-crystal X-ray detectors were shown to have a high sensitivity of $80\ \mu C\ Gy_{air}^{-1}\ cm^{-2}$ to 50 keV X-rays with the lowest detectable dose rate of $0.5\ \mu Gy_{air}\ s^{-1}$, which is already several times more sensitive than the commercial amorphous selenium (α-Se) X-ray detectors[16]. Recently, the integration of perovskite single crystals

[1]Department of Mechanical and Materials Engineering, University of Nebraska-Lincoln, Lincoln, Nebraska 68588, USA. [2]Nuclear Engineering Program, Department of Mechanical and Aerospace Engineering, Ohio State University, Columbus, Ohio 43210, USA. [3]Optoelectronic Materials Section, Department of Chemical Engineering, Delft University of Technology, 2628 BL Delft, the Netherlands. [4]Department of Applied Physical Sciences, University of North Carolina, Chapel Hill, North Carolina 27599, USA. [†]These authors contributed equally to this work. *e-mail: jhuang2@unl.edu

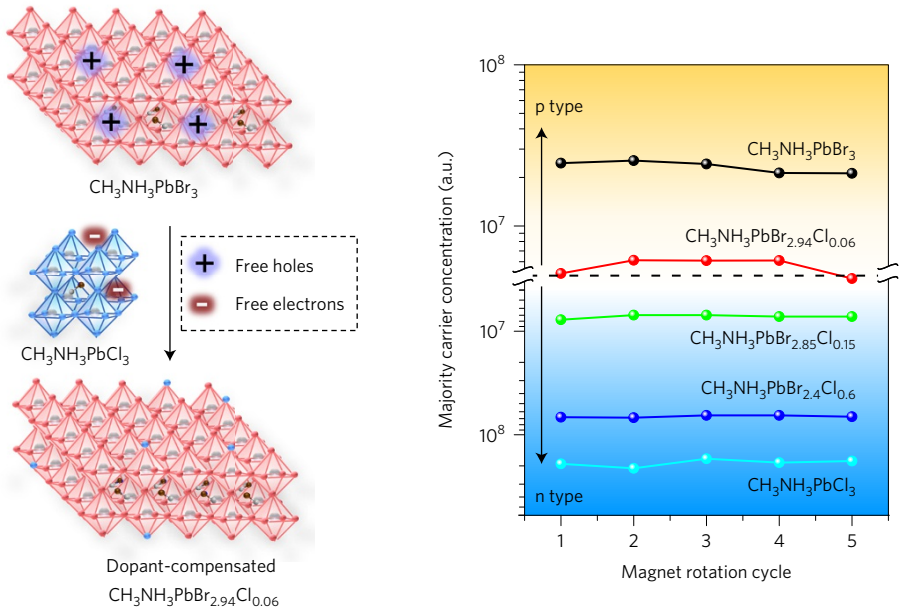

Figure 1 | Cl^- alloying for dopant compensation. a, Scheme of dopant compensation of $CH_3NH_3PbBr_{2.94}Cl_{0.06}$ single crystal. **b**, Hall effect results to reveal the majority carrier type of $CH_3NH_3PbBr_{3-x}Cl_x$ single crystals.

with silicon substrates has been demonstrated, which not only further enhanced the sensitivity to $2.1 \times 10^4\ \mu C\ Gy_{air}^{-1}\ cm^{-2}$ under 8 keV X-ray radiation, but also allowed a direct signal read-out with silicon-based circuits[17]. The demonstrated imaging capability at extremely low dose rates may find its application in medical imaging devices to minimize the X-ray dosage to which patients are exposed. Despite the significant progress made on X-ray detectors operating in current mode, the capability of producing good-resolution energy spectra by perovskite detectors working in pulse-height analysis mode remains a major challenge. Recently, a formamidinium lead triiodide ($FAPbI_3$) single-crystal detector, which is intrinsically not stable at room temperature, was reported to have acquired a 59.6 keV ^{241}Am energy spectrum[13]. However, a high-energy γ-ray spectrum remains unobtainable as a larger size detector is required, by which a high $\mu\tau E$ product (E is the applied electric field) and a large bulk resistivity are desired. A large electric field could be applied to enhance the drift length of charge carriers and reduce their trapping by deep charge traps, but the increased electric field also increases dark current or noise. Therefore, the $\mu\tau$ product of the materials should be large for a strong signal. However, a large mobility also increases dark current, which is proportional to carrier mobility; thus, the direction to reduce dark current noise is to reduce the material's intrinsic charge carrier concentration.

In this article, we report the acquisition of the ^{137}Cs energy spectrum with a low-cost perovskite single-crystal γ-ray detector by suppressing the device's noise while retaining a strong signal with dopant compensation of $CH_3NH_3PbBr_3$. The dopant compensation by Cl^- alloying of p-type $CH_3NH_3PbBr_3$ single crystal dramatically reduces the charge carrier concentration in the bulk crystal, while the carrier mobility and lifetime have been improved significantly, enhancing the charge collection efficiency. In addition, a guard ring electrode was implemented to reduce the surface/edge leakage current that could otherwise corrupt the signal. The improved signal/noise ratio resulted in a well-defined ^{137}Cs energy spectrum by operating the device under a low electric field at room temperature.

Dopant compensation to reduce dark current

A minimum dark current is required for a γ-ray detector to count impingent high-energy photons when acquiring an energy spectrum. Despite the bandgap of a semiconductor that sets the lower limit of the carrier concentration, the dark conductivity of single crystals in γ-ray detectors can be many orders of magnitude larger, often originating from unintentional doping effects by defects or impurities. High-purity raw materials or more sophisticated crystal growth processes are generally employed to improve the crystal quality, yet this increases the cost dramatically and limits the throughput of material production. For many materials, including OIHPs, the unintentional doping cannot be completely eliminated by improved crystal growth due to the thermodynamic stability of certain defects, which, in high concentrations, can dominate the device's dark current. Density functional theory calculations predict that Pb^{2+} vacancies and Br^- vacancies are dominant shallow acceptors and shallow donors in $CH_3NH_3PbBr_3$, respectively. Since the formation energy is lower for Pb^{2+} vacancies than for Br^- vacancies in most synthesis conditions, $CH_3NH_3PbBr_3$ is expected to exhibit a weak unipolar p-doping[20]. It should be noted that the defect formation energy is also dependent on the position of the Fermi level. Experimentally, $CH_3NH_3PbBr_3$ single crystals, synthesized by several methods, demonstrate a p-type conduction by Hall-effect measurements with a resistivity of about $2.0 \times 10^8\ \Omega$ cm (ref. 19), which is over tenfold smaller than that of the state-of-the-art CZT single crystals.

Interestingly, we noticed that the as-synthesized $CH_3NH_3PbCl_3$ single crystals are n-type from Hall effect measurements, and thus had a hypothesis that Cl^- ion vacancies may form more easily than Br^- ion vacancies. Since Cl^- ion vacancies are also expected to be shallow donors, it is reasonable to speculate that Cl^- alloying can reduce the hole density and increase the resistivity of the perovskite crystals. This dopant compensation scheme is illustrated in Fig. 1a. To test it, $CH_3NH_3PbBr_{3-x}Cl_x$ single crystals with different Cl^- percentages were grown from solution by the inverse temperature crystallization method[21], where the $Cl^-/(Br^- + Cl^-)$ molar ratio was tuned by changing the feeding ratio of $CH_3NH_3PbBr_3/CH_3NH_3PbCl_3$. The powder X-ray diffraction (XRD) spectra in Fig. 2a show that all of the diffraction peaks gradually shift to larger angles as the Cl^- molar ratio in the precursor solution is increased from 1.37% to 52.7%, indicating a successful incorporation of Cl^- into the lattice. The actual $Cl^-/(Br^- + Cl^-)$ molar ratio in the crystals is calculated on the basis of the shift of the (012) diffraction peak by assuming the effectiveness of Vegard's law[21].

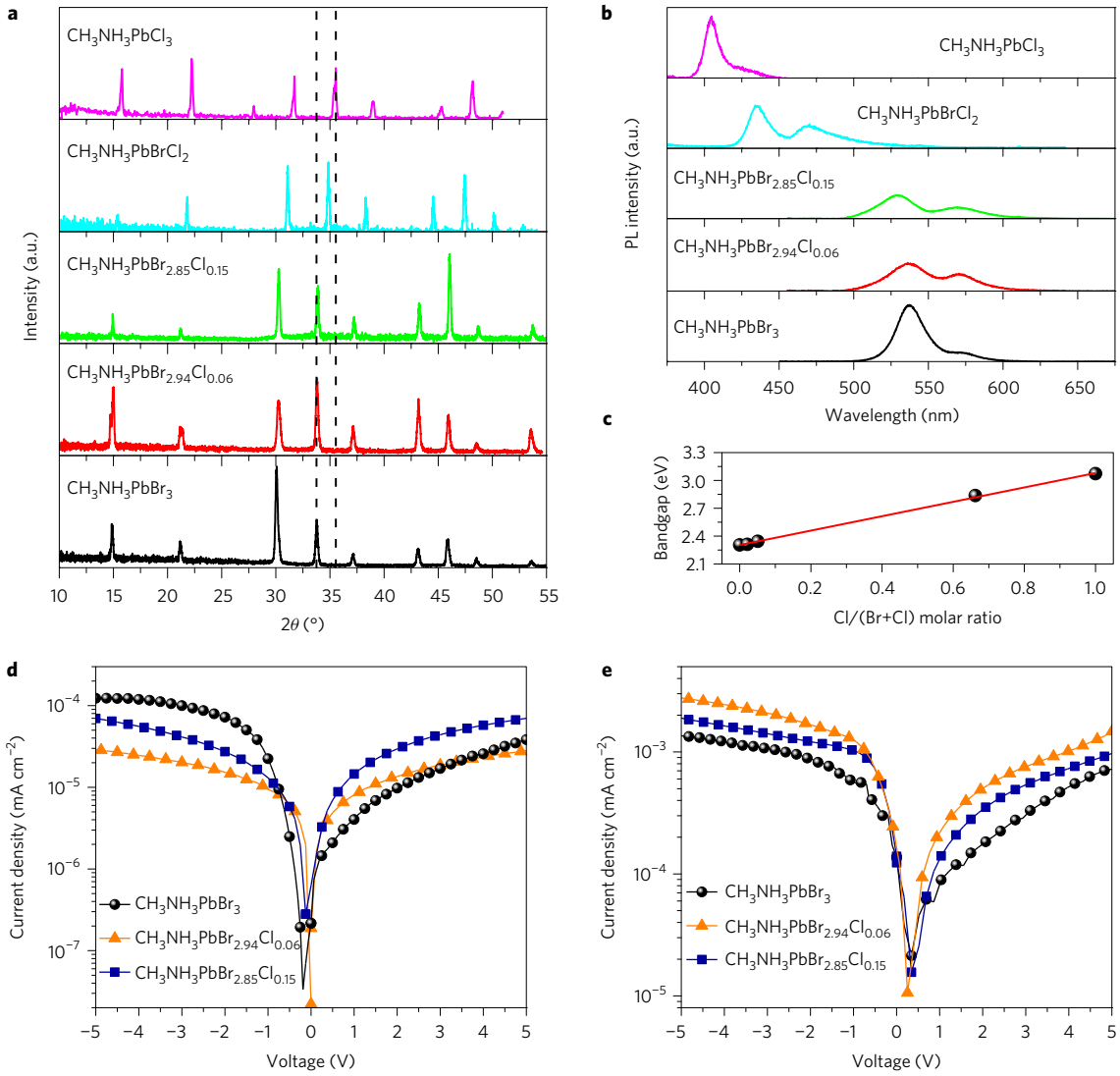

Figure 2 | Cl^- alloying to suppress dark current. a, XRD spectra of $CH_3NH_3PbBr_{3-x}Cl_x$ single-crystal powder with different Cl^- ratios. **b**, Corresponding photoluminescence (PL) spectra of $CH_3NH_3PbBr_{3-x}Cl_x$ single crystals. **c**, Bandgap shift versus Cl/(Br+Cl) ratio. **d**, Dark current density of $CH_3NH_3PbBr_3$, $CH_3NH_3PbBr_{2.94}Cl_{0.06}$ and $CH_3NH_3PbBr_{2.85}Cl_{0.15}$ single-crystal devices with thickness of ~2 mm. **e**, Photocurrent of $CH_3NH_3PbBr_3$, $CH_3NH_3PbBr_{2.94}Cl_{0.06}$ and $CH_3NH_3PbBr_{2.85}Cl_{0.15}$ single-crystal devices under ambient light with thickness of ~2 mm.

The crystals grown with Cl^- feeding ratios of 1.37% and 4.90% have $Cl^-/(Br^- + Cl^-)$ molar ratio of 2.0% and 5.1%, giving compositions of $CH_3NH_3PbBr_{2.94}Cl_{0.06}$ and $CH_3NH_3PbBr_{2.85}Cl_{0.15}$, respectively. In addition, a continuous blueshift of the photoluminescence emission peak was also observed with the increase of the Cl^- ratio, as shown in Fig. 2b. The bandgap derived from the main photoluminescence emission peak presented a linear relationship with the actual $Cl^-/(Br^- + Cl^-)$ molar ratio in the crystals, as shown in Fig. 2c. It is noted that, in photoluminescence emission spectrum, the shoulder peak at longer wavelength range can be assigned to the optical reflection of the photoluminescence from the back surface of the single crystal[22]. After confirming the successful Cl^- alloying, we measured the majority carrier types of the $CH_3NH_3PbBr_{3-x}Cl_x$ single crystals by Hall effect, and verified that addition of Cl^- into the p-type $CH_3NH_3PbBr_3$ converted the crystals to n-type when 20% of Cl^- was added, while $CH_3NH_3PbBr_{2.94}Cl_{0.06}$ is very close to being intrinsic, as shown in Fig. 1b.

We then directly compared the conductivity of a $CH_3NH_3PbBr_{2.94}Cl_{0.06}$ single crystal with a control $CH_3NH_3PbBr_3$ single crystal that has a similar thickness of about 2 mm. A device structure of Cr/$CH_3NH_3PbBr_{3-x}Cl_x$/C_{60}/bathocuproine (BCP)/Cr was used. Figure 2d shows that the dark current density of the $CH_3NH_3PbBr_{2.94}Cl_{0.06}$ device under −5 V is more than five times smaller than that of the control $CH_3NH_3PbBr_3$ device, indicating that the p-type-doped $CH_3NH_3PbBr_3$ is effectively compensated by Cl^- alloying. It should be noted here that only a small portion of the alloyed Cl^- ions contributed to the dopant compensation, while further alloying Cl^- ions to the $CH_3NH_3PbBr_{2.85}Cl_{0.15}$ device results in an increased dark current compared with the dark current of $CH_3NH_3PbBr_{2.94}Cl_{0.06}$ devices. The electronic conductivity of a semiconductor is determined by the product of free charge carrier concentration and carrier mobility (μ). The objective of dopant compensation is to reduce the concentration of free charges, but not the carrier mobility, which would otherwise compromise the device's responsivity. Encouragingly, it is found that the dopant compensation did not sacrifice the responsivity of the $CH_3NH_3PbBr_{2.94}Cl_{0.06}$ devices. As shown in Fig. 2e, the photocurrent of the $CH_3NH_3PbBr_{2.94}Cl_{0.06}$ device under ambient light with intensity of $\sim 2 \times 10^{-4}$ W cm^{-2} is slightly larger than both of the $CH_3NH_3PbBr_3$ and $CH_3NH_3PbBr_{2.85}Cl_{0.15}$ devices, indicating a more efficient collection of photo-generated charges. Four $CH_3NH_3PbBr_{2.94}Cl_{0.06}$ devices were measured to verify the repro-

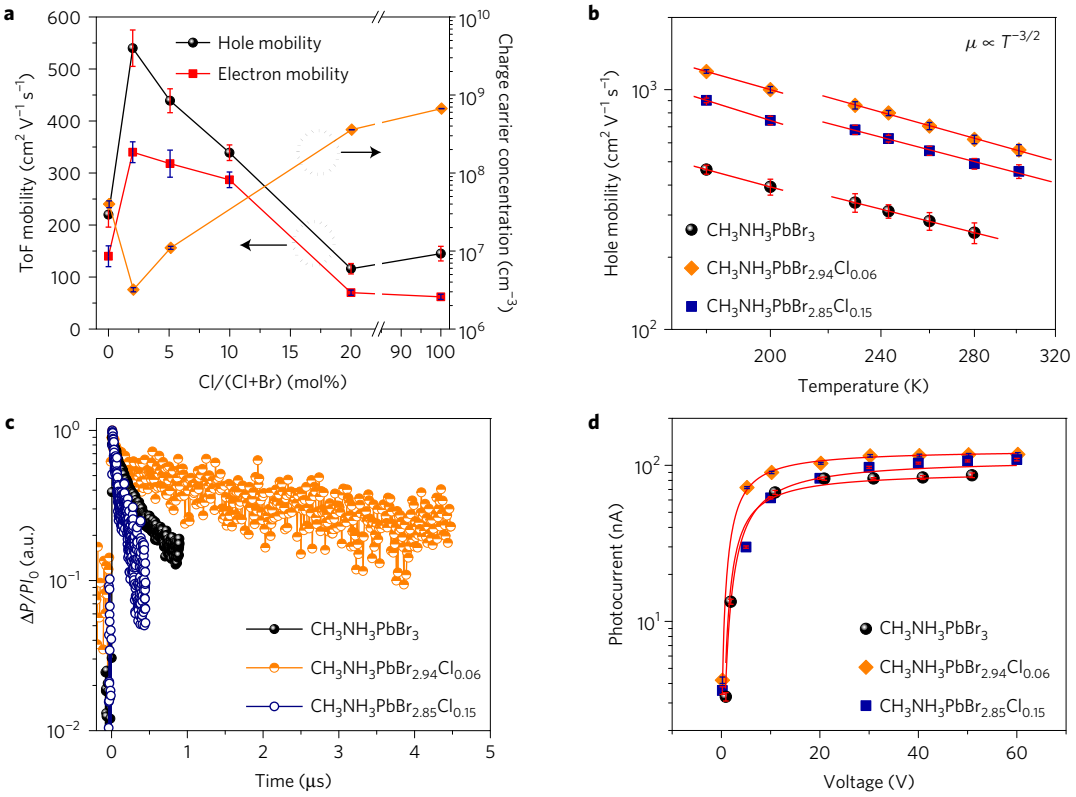

Figure 3 | Mobility and $\mu\tau$ product improvement. a, Hole and electron mobilities of the $CH_3NH_3PbBr_{3-x}Cl_x$ single crystals by ToF technique. Error bars are given according to the variation of single-crystal thicknesses. **b**, Hole mobility of $CH_3NH_3PbBr_{3-x}Cl_x$ single crystals versus temperature. **c**, Time-resolved microwave conductance traces of the $CH_3NH_3PbBr_{3-x}Cl_x$ single crystals. **d**, Photoconductivity of the $CH_3NH_3PbBr_{2.94}Cl_{0.06}$ single crystal with a thickness of ~2 mm.

ducibility of electronic properties of these crystals. The dark current and photocurrent of the devices almost overlap with each other, confirming the good reproducibility (see Supplementary Fig. 1).

Increased carrier mobility and lifetime

We further studied the charge carrier mobility in the single crystals to understand the improved charge collection efficiency. The electron and hole mobilities of $CH_3NH_3PbBr_{3-x}Cl_x$ single crystals were measured by the time-of-flight (ToF) technique. Here, C_{60} and BCP were subsequently deposited on the cathode side as an electron-accepting/transporting layer, thereby enabling a fast extraction of photon-generated electrons as well as the reduction of charge injection under reverse bias. Figure 3a shows that the ToF hole mobility of the $CH_3NH_3PbBr_3$ single crystal is about $220 \pm 20\,cm^2\,V^{-1}\,s^{-1}$ at room temperature, which agrees with previously reported results[16]. The addition of 2.0% Cl^- into $CH_3NH_3PbBr_3$ dramatically increased the hole mobility to $560 \pm 46\,cm^2\,V^{-1}\,s^{-1}$. Further increasing the Cl^- percentage to 20% reduced the hole mobility to $130 \pm 15\,cm^2\,V^{-1}\,s^{-1}$, which is comparable to that of the $CH_3NH_3PbCl_3$ single crystal. The ToF curves of the single-crystal devices with 0%, 2.0% and 5.1% Cl^- alloying are shown in Supplementary Fig. 2, and the corresponding electronic property statistic distribution of four devices for each composition is described in Supplementary Fig. 3. Electron mobility followed the same trend as the hole mobility. The ToF electron mobility of $CH_3NH_3PbBr_3$ single crystal is roughly $140 \pm 17\,cm^2\,V^{-1}\,s^{-1}$, and increases to $340 \pm 20\,cm^2\,V^{-1}\,s^{-1}$ for crystals with 2.0% Cl^- alloying, and then gradually decreases to $320 \pm 30\,cm^2\,V^{-1}\,s^{-1}$ for 5.1% Cl^- alloying of a single crystal (ToF curves are shown in Supplementary Fig. 2). Therefore, the dopant-compensated crystal has both the highest hole and electron mobility. Although the electron mobility is slightly lower than the hole mobility, they are still within the same order of magnitude. The ToF electron mobility is also in accordance with the mobility measured by the space-charge-limited current (Supplementary Fig. 4).

High-quality perovskite single crystals provide a platform to study the intrinsic mobility of perovskite due to the absence of grain boundary[16,19,23,24]. The carrier mobility is determined by the carrier's effective mass (m^*) and the average scattering (or momentum relaxation) time (τ') via the relationship $\mu = e\tau'/m^*$, where e is the elementary charge[25,26]. The calculated effective mass of $CH_3NH_3PbBr_3$ is comparable to that of silicon[27], giving the materials a potential to exhibit a large mobility of over $1{,}000\,cm^2\,V^{-1}\,s^{-1}$ at room temperature, which is greater than the previously measured values[28,29]. The enhanced carrier mobility indicates that the carrier scattering caused by dopants or charged centres may be limiting the carrier mobility in perovskite. Calculation results predicted that Cl^- alloying in I^--based perovskite would extend the carrier's thermalization time[30], which was mainly caused by the structural deformation of PbI_6^{4-} octahedra and lattice parameter changes after Cl^- alloying. To identify the relationship between temperature and carrier scattering, the temperature-dependent ToF hole mobility of $CH_3NH_3PbBr_{3-x}Cl_x$ single crystals was measured from 300 K to 180 K, with the results displayed in Fig. 3b (ToF curves are shown in Supplementary Figs 5–7). With the exception of a discontinuity at 225 K, the mobilities presented a clear $T^{-1.5}$ dependence for all three single-crystal devices at temperatures both above and below the cubic phase to tetragonal phase transition temperature (225 K) (ref. 31). Therefore, the high hole mobility of $560 \pm 46\,cm^2\,V^{-1}\,s^{-1}$ at 300 K and $\sim 1{,}200 \pm 50\,cm^2\,V^{-1}\,s^{-1}$ at 180 K provides evidence of the increased electronic quality of the $CH_3NH_3PbBr_{2.94}Cl_{0.06}$ single crystals.

The reduction of the charged dopant centre may also impact the charge carrier recombination process. As presented in Fig. 3c, the

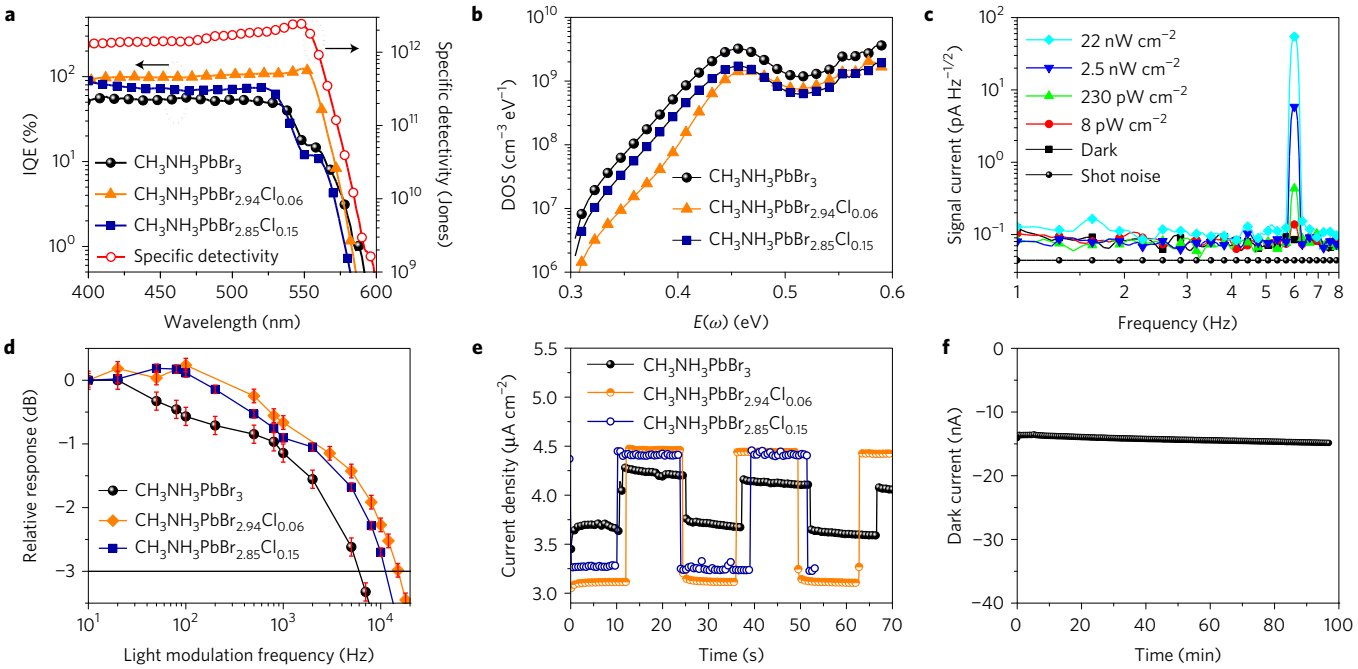

Figure 4 | Photodetector performance. a, IQE of the $CH_3NH_3PbBr_{3-x}Cl_x$ single-crystal devices and specific detectivity of the $CH_3NH_3PbBr_{2.94}Cl_{0.06}$ single-crystal device under −5 V with a thickness of ∼2.4 mm. **b**, Trap density of states of the $CH_3NH_3PbBr_{3-x}Cl_x$ single-crystal devices with different Cl^- ratios. **c**, Noise current and directly measured NEP of the $CH_3NH_3PbBr_{2.94}Cl_{0.06}$ single-crystal device with a thickness of ∼2.4 mm under −5 V. **d**, Temporal response of the $CH_3NH_3PbBr_{3-x}Cl_x$ single-crystal device with a thickness of ∼2.4 mm under −5 V. Error bars are given according to the variation of photocurrent signal. **e**, Dark current and photocurrent stability of the $CH_3NH_3PbBr_{3-x}Cl_x$ single-crystal device under electrical field of 0.11 V μm^{-1}. **f**, Long-term dark current stability of the $CH_3NH_3PbBr_{2.94}Cl_{0.06}$ single-crystal device under electrical field of 1.8 V mm^{-1}.

carrier recombination lifetime in the single crystals was studied by time-resolved microwave conductance, where a 570 nm laser pulse was utilized to generate free charges. Since photons with 570 nm wavelength can fully penetrate the bulk of the single crystal, charges are generated not only at the surface but also inside the single crystal. A weak nanosecond laser pulse of 5.4×10^{13} photons per square centimetre per pulse was successfully used for excitation. A lifetime of ∼5 μs was recorded for the $CH_3NH_3PbBr_{2.94}Cl_{0.06}$ single crystals, which is a tenfold increase as compared with that of $CH_3NH_3PbBr_3$ and $CH_3NH_3PbBr_{2.85}Cl_{0.15}$ single crystals. Since the charge recombination lifetime is strongly dependent on the photo-generated carrier concentration, we continued to evaluate the $\mu\tau$ product at even weaker light intensities to emulate the working condition of the devices under naturally occurring gamma radiation. As seen in Fig. 3d, the steady-state photoconductivity curve of the $CH_3NH_3PbBr_{2.94}Cl_{0.06}$ single crystal, induced by a 1.2×10^{12} photons cm^{-2} s^{-1} light source, reveals a $\mu\tau$ product of $(1.8 \pm 0.2) \times 10^{-2}$ cm^2 V^{-1} as well as an extremely low surface recombination velocity of 55 cm s^{-1}. The $\mu\tau$ product is larger than that of $CH_3NH_3PbBr_{2.85}Cl_{0.15}$ single crystals ($(1.5 \pm 0.2) \times 10^{-2}$ cm^2 V^{-1}) and $CH_3NH_3PbBr_3$ single crystals ($(1.1 \pm 0.2) \times 10^{-2}$ cm^2 V^{-1}).

Photon detection performance

With increased carrier mobility and recombination lifetime, we hypothesize that the charge collection would be improved in $CH_3NH_3PbBr_{2.94}Cl_{0.06}$ detectors compared with the $CH_3NH_3PbBr_3$ or $CH_3NH_3PbBr_{2.85}Cl_{0.15}$ detectors. Therefore, to characterize the charge collection efficiency (CCE) or the internal quantum efficiency (IQE), the external quantum efficiency (EQE) of the $CH_3NH_3PbBr_{2.94}Cl_{0.06}$ single-crystal device was measured under a reverse bias. The CCE was then equated as the ratio of the EQE to the electrode transparency. As shown in Fig. 4a, the CCE of the 2.4-mm-thick $CH_3NH_3PbBr_{2.94}Cl_{0.06}$ single-crystal device reached 100% under a −5 V, slightly better than that of the $CH_3NH_3PbBr_{2.85}Cl_{0.15}$ device, but twofold larger than that of the $CH_3NH_3PbBr_3$ device, which can be attributed to the larger $\mu\tau$ product and thus longer drift length of $CH_3NH_3PbBr_{2.94}Cl_{0.06}$ single crystal. The frequency response of the $CH_3NH_3PbBr_{2.94}Cl_{0.06}$ single crystal under −5 V can be seen in Fig. 4d, in which the bandwidth is evaluated as 15.2 kHz. This in turn corresponds to a response time of 23 μs, which is close to the calculated transit time of 21 μs by a hole mobility of 560 cm^2 V^{-1} s^{-1}. Here the transit time is calculated by $t = d^2/\mu V$, where d is the thickness and V is the applied voltage. In addition to high mobility, the $CH_3NH_3PbBr_{2.94}Cl_{0.06}$ single crystals should also have a low charge trap density; otherwise a fast response time would be unlikely given the long charge trapping and detrapping time from the deep traps. The thermal admittance spectroscopy measurement provides the trap density of states in the single-crystal devices, as shown in Fig. 4b. The dopant-compensated $CH_3NH_3PbBr_{2.94}Cl_{0.06}$ device has nearly a tenfold reduction of charge traps when compared with the $CH_3NH_3PbBr_3$ single-crystal device. Such a reduction can be attributed to the compensation of the p-type dopants. It is noted that while the trap density remains unchanged for the $CH_3NH_3PbBr_{2.85}Cl_{0.15}$ single-crystal device when considering the deep trap depth, it is slightly higher in the shallow trap depth range, which may be caused by the additional Cl^- n-type dopant.

Just as both low trap density and device dark current are crucial factors on the performance of weak-light-sensitive photodetectors, so too are they important factors on the performance of high-energy γ-ray detectors. One of the most important figures of merit for a photodetector is the noise equivalent power (NEP), which characterizes its capability to detect low-intensity light[32]. Therefore, the NEP was evaluated by directly measuring the lowest detectable light intensity. In Fig. 4c, the frequency-independent noise current of the $CH_3NH_3PbBr_{2.94}Cl_{0.06}$ single-crystal device at −5 V is roughly 0.085 pA $Hz^{-1/2}$. The lowest distinguishable light intensity is then

8 pW cm^{-2}, which in turn converts to a NEP of 1.3 pW Hz$^{-1/2}$, comparable to the calculated NEP of 2 pW Hz$^{-1/2}$ from device responsivity and directly measured noise. A high specific detectivity D^* of 2.5×10^{12} jones was derived from the IQE and measured noise current. It is noted that IQE is used here for evaluation, because high-energy photons can easily penetrate the thin metal electrode. Finally, the device's response to X-rays with varying dose rates was also measured. The device sensitivity to 8 keV X-rays was derived from the slope of the straight line of the output current density versus the X-ray dose, which reaches 8.4×10^4 μC Gy_{air}^{-1} cm^{-2} with the lowest detectable dose rate of 7.6 nGy_{air} s^{-1}, which is about 4,000-fold better than that of commercial α-Se X-ray detectors[33] (Supplementary Fig. 8a,b).

γ-ray energy spectrum detection

One major concern for the application of OIHP materials for radiation detection is the polarization effect due to ion migration, which would result in a shift of the energy spectrum as well as a degradation of resolution[34]. Furthermore, ion migration in OIHP polycrystalline films has been known to result in a switchable photovoltaic effect[35] as well as be an origin of the current hysteresis phenomenon in OIHP devices[36]. Despite the ion migration through grain interiors, we have revealed that grain boundaries in polycrystalline films are faster ion migration channels[37]. Therefore, the absence of grain boundaries in high-quality single crystals should suppress the polarization effect. Nevertheless, we still observed a small drift of both the dark current and photocurrent for the control $CH_3NH_3PbBr_3$ single-crystal device under an applied electric field of 0.11 V μm^{-1} (Fig. 4e), which may be caused by ion migration along the crystal surface or possibly by charge trapping/detrapping effects. The $CH_3NH_3PbBr_{2.94}Cl_{0.06}$ single-crystal device demonstrated an enhanced stability for both the dark current and photocurrent under the same electric field. In practice, the excellent charge collection efficiency and response speed enable our detector to work under a low electric field of 1.8 V mm^{-1}, which retains a stabilized small dark current. We continuously monitored the dark current under the electric field of 1.8 V mm^{-1} for about 100 min, and found that the dark current drifted only ∼1 nA cm^{-2}, or 8% of the dark current (Fig. 4f). The increased stability may be attributed to the increased attraction forces between the cation–anion pair of the Cl^- anions as compared with the Br^- anions. The increased attraction would in effect suppress ion migration through the crystal surface, agreeing with the reduced trap density measured.

Despite the reduction of polarization effects, the $CH_3NH_3PbBr_{2.94}Cl_{0.06}$ single crystals maintain several defects on the crystal surface, resulting in a significant surface leakage current. Such leakage current is only notable when the bulk resistivity of the crystal is very large so that the bulk leakage current is comparable or smaller[38]. To mitigate the leakage current, a guard ring electrode was employed around the central cathode as illustrated in Fig. 5a. The central cathode and the guard electrode are separated by a channel of 50 μm. The photos of the guard ring electrode, the back electrode, and the whole device after encapsulation are shown in Fig. 5b–d. The electric field between the guard electrode and anode can be the same as that between the central cathode and anode[38,39]. In this way, the surface/edge leakage current is absorbed by the outer guard electrode while the main signal is produced from flow of inner bulk charges. Figure 5e demonstrates the resulting fourfold suppression of the dark current from the guard ring electrode device. The intrinsic resistivity of the $CH_3NH_3PbBr_{2.94}Cl_{0.06}$ single crystal reaches 3.6×10^9 Ω cm, comparable to the state-of-the-art CZT materials[8]. The high resistivity comes from the low charge carrier concentration of the single crystal. A tenfold reduction in bulk carrier concentration was observed for the $CH_3NH_3PbBr_{2.94}Cl_{0.06}$ single crystal compared with the control $CH_3NH_3PbBr_3$ single crystal by taking the mobility change after dopant compensation into consideration, as shown in Fig. 3a (details of the calculation are presented in Supplementary Table 1), in agreement with the Hall effect result presented in Fig. 1b.

The energy resolution is the most important figure of merit to evaluate how well a detector can resolve the fine energy lines from nuclear decay. A detector for pulse-height analysis should firstly have a large size, or footprint, to stop high-energy γ-ray radiation and secondly, a large $\mu\tau E$ product, that is, the mean free path of free charge carrier, to outperform the physical length of the detector. We confirmed the $\mu\tau E$ product of our crystals under 1.8 V mm^{-1} is larger than the crystal thickness. Utilizing enhancements by guard rings, the ^{137}Cs energy spectrum was obtained with three $CH_3NH_3PbBr_{2.94}Cl_{0.06}$ single-crystal devices (named as device I, II and III). The crystals I, II and III have dimensions of $1.30 \times 1.25 \times 0.37$ cm^3, $1.44 \times 1.37 \times 0.58$ cm^3, and $1.06 \times 1.00 \times 0.49$ cm^3, respectively, and a photo of single crystal II is shown in the inset of Fig. 5e. A 5.0 μCi ^{137}Cs source was placed 10 cm from the anode of the $CH_3NH_3PbBr_{2.94}Cl_{0.06}$ detector, which was connected to a charge-sensitive preamplifier (Ortec-142A) and processed with a DSP (Ortec DSPEC 50). A typical ^{137}Cs energy spectrum was acquired by the $CH_3NH_3PbBr_{2.94}Cl_{0.06}$ (device I) detector under an electric field of 1.8 V mm^{-1} at room temperature as shown in Fig. 5f, and two other spectra collected by two other $CH_3NH_3PbBr_{2.94}Cl_{0.06}$ detectors are shown in Fig. 5g (device II) and Fig 5h and Supplementary Fig. 9b (device III). Although each perovskite device has shown a different energy resolution and photopeak to Compton ratio[40], which might be related to variation of contact qualities, the spectrum features, such as the Compton edge with respect to its energy, are consistently aligned with the theoretical value and the energy scale calibrated by reference detectors. As a comparison, no photopeak or Compton edge was observed in the ^{137}Cs energy spectrum acquired by any $CH_3NH_3PbBr_3$ device, as shown in Fig. 5g, indicating the important role of high mobility and low free carrier concentration of $CH_3NH_3PbBr_{2.94}Cl_{0.06}$ for spectrum collection. A CZT semiconductor detector (1.0 cm^3 volume) and a NaI(Tl) scintillator (a cylinder of 7.62 cm diameter and 7.62 cm tall)-based detector were used for reference. As can be seen in Fig. 5f, the photopeak to Compton ratio is lower for $CH_3NH_3PbBr_{2.94}Cl_{0.06}$ than that of the CZT and NaI(Tl) reference detectors. This is mainly due to its small size, allowing a large fraction of Compton scattered photons to escape. It also partially owes to the small electric field that results in a long average electron transit time of 13 μs as compared with the charge carrier recombination lifetime of about 32 μs. Nevertheless, $CH_3NH_3PbBr_{2.94}Cl_{0.06}$ perovskite single crystal demonstrates desirable material properties for a good-resolution gamma spectroscopy, for instance, a large ratio of photoelectric to total cross-section, σ_{pe}/σ_{tot}, 0.24 at 662 keV as compared with CZT's ratio of 0.08 (ref. 41). This, in theory, presents perovskite the potential to obtain a more prominent photopeak than an industry-leading room-temperature gamma-ray detector. The typical resolution of $CH_3NH_3PbBr_{2.94}Cl_{0.06}$ detectors is around 12%, while the best $CH_3NH_3PbBr_{2.94}Cl_{0.06}$ device has a resolution of 6.50% (Fig. 5g). In comparison, the resolutions of the full-energy peaks are 2.27%, and 7.51% for CZT and NaI(Tl), respectively (Fig. 5f). It is shown that perovskite is capable of obtaining a resolution better than that obtained through a typical NaI(Tl) scintillator detector while being much more economical than standard semiconductor detectors used in industry. We estimated the raw material cost of $CH_3NH_3PbBr_{2.94}Cl_{0.06}$ single crystals to be less than US$0.3 cm^{-3} (see Supplementary Information). Moreover, the ability to grow high-quality perovskite crystals larger than 1.0 cm^3 provides the potential for increased efficiency/cost ratio, which limits other semiconductor detectors such as CZT.

Finally, we studied the stability of the $CH_3NH_3PbBr_{2.94}Cl_{0.06}$ single-crystal detector using device III by measuring the variation of device charge collection efficiency and dark current over time.

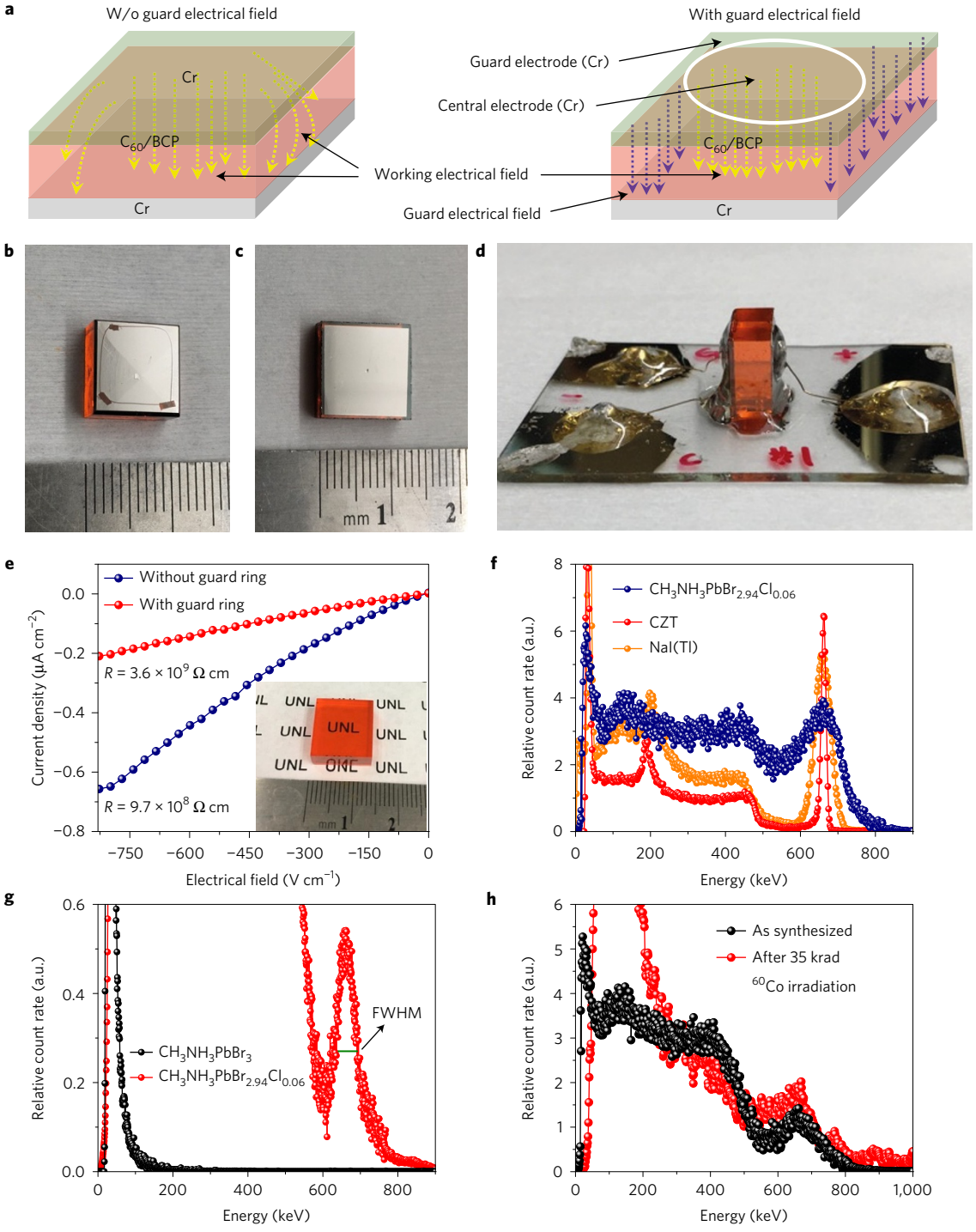

Figure 5 | γ-ray detector performance. a, Electric field distribution of a single-crystal device with a guard electrode. **b**, Top view of the guard ring electrode side of the detector. **c**, Top view of the anode side of the detector. **d**, Side view of a $CH_3NH_3PbBr_{2.94}Cl_{0.06}$ single-crystal detector, and electrode sides were encapsulated with epoxy. **e**, Dark current density of a $CH_3NH_3PbBr_{2.94}Cl_{0.06}$ single-crystal device with and without a guard ring. The thickness of this device is ~5.8 mm. Inset is a photograph of a centimetre-sized $CH_3NH_3PbBr_{2.94}Cl_{0.06}$ single crystal for ^{137}Cs energy spectrum with dimension of $1.44 \times 1.37 \times 0.58\ cm^3$. **f**, ^{137}Cs energy spectrum obtained by $CH_3NH_3PbBr_{2.94}Cl_{0.06}$ (device I), CZT and NaI(Tl) detectors. **g**, Enlarged photopeak region of the ^{137}Cs energy spectrum obtained by $CH_3NH_3PbBr_{2.94}Cl_{0.06}$ (device II) and $CH_3NH_3PbBr_3$ single-crystal detectors. FWHM, full width at half maximum. **h**, ^{137}Cs energy spectrum obtained by $CH_3NH_3PbBr_{2.94}Cl_{0.06}$ (device III) before and after 35 krad ^{60}Co irradiation.

Supplementary Fig. 10 shows that the $CH_3NH_3PbBr_{2.94}Cl_{0.06}$ single-crystal device has a good shelf stability with almost no change of IQE and dark current after one-month storage in air without any encapsulation. In addition, it also exhibits a very good radiation resistance. As shown in Fig. 5h, the gamma-ray spectrum shows similar resolution and no shift of photopeaks after ^{60}Co irradiation at an accumulated dose of 35 krad, equivalent to about 3.5 million times the dosage received during a chest X-ray exam. The excellent radiation hardness of perovskite can be ascribed to the defect tolerance of hybrid perovskite materials, because most of the radiation-induced point defects do not cause deep charge traps in these materials[18].

In conclusion, high-quality and dopant-compensated $CH_3NH_3PbBr_{2.94}Cl_{0.06}$ single crystals were grown by low-cost solution processes resulting in an about threefold improvement of mobility to a high value of $560\,cm^2\,V^{-1}\,s^{-1}$. Additionally, a tenfold reduction of dark current was achieved in comparison to pure $CH_3NH_3PbBr_3$ single crystals. The $\mu\tau$ product reached a large value of $1.8 \times 10^{-2}\,cm^2\,V^{-1}$. Surface edge leakage current of $CH_3NH_3PbBr_{2.94}Cl_{0.06}$ single crystals was effectively suppressed by employing a guard ring electrode, which revealed a bulk resistivity of $3.6 \times 10^9\,\Omega\,cm$. A well-defined ^{137}Cs energy spectrum was obtained by using a $CH_3NH_3PbBr_{2.94}Cl_{0.06}$ single crystal under a small electric field of $1.8\,V\,mm^{-1}$ at room temperature. Consequently, the obtained energy spectrum demonstrated a comparable or better resolution than that of a standard scintillator detector. The gamma spectrum presented here is the experimental evidence of how a large-sized perovskite single crystal can successfully detect the charge produced by the ionization. The low-cost, easy material synthesis, and good radiation hardness of the hybrid perovskites make them promising candidates for the next generation of radiation detector materials.

Methods

Methods, including statements of data availability and any associated accession codes and references, are available in the online version of this paper.

Received 2 March 2017; accepted 26 May 2017;
published online 3 July 2017

References

1. Kasap, S. *et al*. Amorphous and polycrystalline photoconductors for direct conversion flat panel X-ray image sensors. *Sensors* **11,** 5112–5157 (2011).
2. Yamamoto, Y. & Shinohara, K. Application of X-ray microscopy in analysis of living hydrated cells. *Anat. Rec.* **269,** 217–223 (2002).
3. Büchele, P. *et al*. X-ray imaging with scintillator-sensitized hybrid organic photodetectors. *Nat. Photon.* **9,** 843–848 (2015).
4. Johns, P. M., Baciak, J. E. & Nino, J. C. Enhanced gamma ray sensitivity in bismuth triiodide sensors through volumetric defect control. *Appl. Phys. Lett.* **109,** 092105 (2016).
5. Venkataraman, R., Croft, S. & Russ, W. R. Calculation of peak-to-total ratios for high purity germanium detectors using Monte-Carlo modeling. *J. Radioanal. Nucl. Chem.* **264,** 183–191 (2005).
6. Szeles, C. CdZnTe and CdTe materials for X-ray and gamma ray radiation detector applications. *Phys. Status Solidi b* **241,** 783–790 (2004).
7. Schlesinger, T. E. *et al*. Cadmium zinc telluride and its use as a nuclear radiation detector material. *Mater. Sci. Eng. R* **32,** 103–189 (2001).
8. Del Sordo, S. *et al*. Progress in the development of CdTe and CdZnTe semiconductor radiation detectors for astrophysical and medical applications. *Sensors* **9,** 3491–3526 (2009).
9. Liu, M., Johnston, M. B. & Snaith, H. J. Efficient planar heterojunction perovskite solar cells by vapour deposition. *Nature* **501,** 395–398 (2013).
10. Wang, Q. *et al*. Thin insulating tunneling contacts for efficient and water-resistant perovskite solar cells. *Adv. Mater.* **28,** 6734–6739 (2016).
11. Stranks, S. D. & Snaith, H. J. Metal-halide perovskites for photovoltaic and light-emitting devices. *Nat. Nanotech.* **10,** 391–402 (2015).
12. Fang, Y. J. *et al*. Highly narrowband perovskite single-crystal photodetectors enabled by surface-charge recombination. *Nat. Photon.* **9,** 679–686 (2015).
13. Yakunin, S. *et al*. Detection of gamma photons using solution-grown single crystals of hybrid lead halide perovskites. *Nat. Photon.* **10,** 585–589 (2016).
14. Yakunin, S. *et al*. Detection of X-ray photons by solution-processed lead halide perovskites. *Nat. Photon.* **9,** 444–449 (2015).
15. Dong, Q. *et al*. Electron-hole diffusion lengths >175 μm in solution-grown $CH_3NH_3PbI_3$ single crystals. *Science* **347,** 967–970 (2015).
16. Wei, H. *et al*. Sensitive X-ray detectors made of methylammonium lead tribromide perovskite single crystals. *Nat. Photon.* **10,** 333–339 (2016).
17. Wei, W. *et al*. Monolithic integration of hybrid perovskite single crystals with heterogenous substrate for highly sensitive X-ray imaging. *Nat. Photon.* **11,** 315–321 (2017).
18. Yin, W.-J., Shi, T. & Yan, Y. Unusual defect physics in $CH_3NH_3PbI_3$ perovskite solar cell absorber. *Appl. Phys. Lett.* **104,** 063903 (2014).
19. Shi, D. *et al*. Low trap-state density and long carrier diffusion in organolead trihalide perovskite single crystals. *Science* **347,** 519–522 (2015).
20. Shi, T. *et al*. Unipolar self-doping behavior in perovskite $CH_3NH_3PbBr_3$. *Appl. Phys. Lett.* **106,** 103902 (2015).
21. Noh, J. H. *et al*. Chemical management for colorful, efficient, and stable inorganic–organic hybrid nanostructured solar cells. *Nano Lett.* **13,** 1764–1769 (2013).
22. Fang, Y., Wei, H., Dong, Q. & Huang, J. Quantification of re-absorption and re-emission processes to determine photon recycling efficiency in perovskite single crystals. *Nat. Commun.* **8,** 14417 (2017).
23. Saidaminov, M. I. *et al*. High-quality bulk hybrid perovskite single crystals within minutes by inverse temperature crystallization. *Nat. Commun.* **6,** 7586 (2015).
24. Lian, Z. *et al*. Perovskite $CH_3NH_3PbI_3$(Cl) single crystals: rapid solution growth, unparalleled crystalline quality, and low trap density toward $10^8\,cm^{-3}$. *J. Am. Chem. Soc.* **138,** 9409–9412 (2016).
25. Zhu, X. Y. & Podzorov, V. Charge carriers in hybrid organic–inorganic lead halide perovskites might be protected as large polarons. *J. Phys. Chem. Lett.* **6,** 4758–4761 (2015).
26. Yi, H. T., Wu, X., Zhu, X. & Podzorov, V. Intrinsic charge transport across phase transitions in hybrid organo-inorganic perovskites. *Adv. Mater.* **28,** 6509–6514 (2016).
27. Galkowski, K. *et al*. Determination of the exciton binding energy and effective masses for methylammonium and formamidinium lead tri-halide perovskite semiconductors. *Energy Environ. Sci.* **9,** 962–970 (2016).
28. He, Y. & Galli, G. Perovskites for solar thermoelectric applications: a first principle study of $CH_3NH_3AI_3$ (A = Pb and Sn). *Chem. Mater.* **26,** 5394–5400 (2014).
29. Brenner, T. M. *et al*. Are mobilities in hybrid organic–inorganic halide perovskites actually 'high'? *J. Phys. Chem. Lett.* **6,** 4754–4757 (2015).
30. Madjet, M. E.-A. *et al*. Enhancing the carrier thermalization time in organometallic perovskites by halide mixing. *Phys. Chem. Chem. Phys.* **18,** 5219–5231 (2016).
31. Swainson, I. P. *et al*. Phase transitions in the perovskite methylammonium lead bromide, $CH_3ND_3PbBr_3$. *J. Solid State Chem.* **176,** 97–104 (2003).
32. Wei, H. *et al*. Trap engineering of CdTe nanoparticle for high gain, fast response, and low noise P_3HT:CdTe nanocomposite photodetectors. *Adv. Mater.* **27,** 4975–4981 (2015).
33. Kasap, S. O. X-ray sensitivity of photoconductors: application to stabilized a-Se. *J. Phys. D* **33,** 2853–2865 (2000).
34. Leão, C. R. & Lordi, V. Ionic current and polarization effect in TlBr. *Phys. Rev. B* **87,** 081202 (2013).
35. Xiao, Z. *et al*. Giant switchable photovoltaic effect in organometal trihalide perovskite devices. *Nat. Mater.* **14,** 193–198 (2015).
36. Li, C. *et al*. Iodine migration and its effect on hysteresis in perovskite solar cells. *Adv. Mater.* **28,** 2446–2454 (2016).
37. Shao, Y. *et al*. Grain boundary dominated ion migration in polycrystalline organic-inorganic halide perovskite films. *Energy Environ. Sci.* **9,** 1752–1759 (2016).
38. Nakazawa, K. *et al*. Improvement of the CdTe diode detectors using a guard-ring electrode. *IEEE Trans. Nucl. Sci.* **51,** 1881–1885 (2004).
39. Niraula, M., Agata, Y. & Yasuda, K. Study of multi-electrodes structure in CdTe nuclear radiation detectors. *Nucl. Sci. Symp. Conf. Rec. IEEE* **7,** 4532–4534 (2004).
40. Knoll, G. F. *Radiation Detection and Measurement* (John Wiley, 2010).
41. Berger, M. J. *et al*. *XCOM: Photon Cross Sections Database: NIST Standard Reference Database 8* (NIST, 2013).

Acknowledgements

This work is financially supported by the Defense Threat Reduction Agency (Award No. HDTRA1-14-1-0030). We thank Y. Yan at the University of Toledo for the discussion of the doping mechanism in the mixed-halide perovskites.

Author contributions

J.H. conceived and supervised the project. H.W. synthesized crystals, fabricated the devices, and measured the optoelectronic properties and X-ray detector sensitivity. D.D. performed and L.C. supervised the ^{137}Cs energy spectrum measurement. H.W. and W.W. calibrated the X-ray dose rate. Y.D. carried out the XRD measurement. D.G. and T.J.S. contributed the charge carrier lifetime measurement. J.H., H.W., D.D. and L.C. wrote the manuscript, and all the authors reviewed the manuscript.

Additional information

Supplementary information is available in the online version of the paper. Reprints and permissions information is available online at www.nature.com/reprints. Publisher's note: Springer Nature remains neutral with regard to jurisdictional claims in published maps and institutional affiliations. Correspondence and requests for materials should be addressed to J.H.

Competing financial interests

The authors declare no competing financial interests.

Methods

Materials. The materials used were as follows: lead bromide ($PbBr_2$) (>98%, Sigma-Aldrich), lead chloride ($PbCl_2$) (>98%, Sigma-Aldrich), methylamine (CH_3NH_2) (40% w/w aq. soln., Alfa Aesar), hydrobromic acid (HBr) (48% w/w aq. soln., Alfa Aesar), hydrochloric acid (HCl) (36.5 wt% in water, Alfa Aesar), C_{60} (>99.5%, Nano-C), BCP (>96%, Sigma-Aldrich), *N,N*-dimethylformamide (DMF) (>99.8%, Alfa Aesar), dichloromethane (DCM) (99.7%, Alfa Aesar).

Synthesis of methylammonium bromide (CH_3NH_3Br). CH_3NH_3Br was prepared by slowly mixing methylamine with HBr in a 1:1 molar ratio under continuous stirring at 0 °C for 2 h. CH_3NH_3Br was then crystallized by removing the solvent from an evaporator, washing three times in diethyl ether, and filtering the precipitate. The white crystal was obtained by recrystallization with ethanol, then dried in vacuum for 24 h, and kept in a dark and dry environment for further use.

Synthesis of methylammonium chloride (CH_3NH_3Cl). CH_3NH_3Cl was synthesized by the reaction of methyl-amine (13.5 ml) with a concentrated aqueous solution of hydrochloric acid (23.5 ml) at 0 °C for 2 h with constant stirring, followed by a crystallization purification and drying process.

Growth of $CH_3NH_3PbBr_3$ single crystal (SC). 1.5 M $PbBr_2$ and 1.5 M CH_3NH_3Br were dissolved in DMF solution in a vial to keep the molar ratio of $PbBr_2$ to CH_3NH_3Br as 1. Then the solution was heated on a hot plate. Finally, $CH_3NH_3PbBr_3$ single crystals were slowly grown by gradually increasing the temperature of the hot plate.

Growth of $CH_3NH_3PbCl_3$ single crystal. 1 M $CH_3NH_3PbCl_3$ solution in DMSO–DMF (1:1 by volume) was prepared by dissolving equimolar amounts of CH_3NH_3Cl and $PbCl_2$. The solution was then filtered using a PTFE filter. We grew single crystals from this solution by gradually increasing the temperature.

Growth of $CH_3NH_3PbBr_{3-x}Cl_x$ single crystal. $CH_3NH_3PbBr_{3-x}Cl_x$ single crystals were grown either by an anti-solvent method or an inverse temperature crystalline method. For the inverse temperature crystalline method: 1.5 M $PbBr_2$ and 1.5 M CH_3NH_3Br were dissolved in DMF solution in a vial to get $CH_3NH_3PbBr_3$ solution, and $CH_3NH_3PbCl_3$ single crystal with different amounts (2.0% or 5.1%, mol%) was dissolved in this solution under long-term stirring. Then the solution was heated on a hot plate. Finally, $CH_3NH_3PbBr_{3-x}Cl_x$ single crystals were slowly grown by gradually increasing the temperature of the hot plate; for the anti-solvent method: 1 M $PbBr_2$ and 1 M CH_3NH_3Br were dissolved in DMF solution in a vial to get $CH_3NH_3PbBr_3$ solution, and $CH_3NH_3PbCl_3$ single crystal with different amounts (2.0% or 5.1%, mol%) was dissolved in this solution under long-term stirring. Then the vial was sealed with aluminium foil but leaving a small hole, and the vial was stored under DCM atmosphere. Finally, $CH_3NH_3PbBr_{3-x}Cl_x$ single crystals slowly grew big in several days.

Device fabrication. 20 nm Cr was deposited on the top surface of the single crystal as the anode; then on the bottom surface, electron-transporting layers were constructed by depositing 20 nm C_{60} and 8 nm BCP. Finally, 20 nm Cr was employed as a semi-transparent cathode by using a thermal evaporation system through a shadow mask under high vacuum. The guard ring electrode was deposited by thermal evaporation together with the central cathode, and the central cathode and the guard electrode were separated by a mask with channel width of 50 μm. The electrode was also extended to a substrate, where the external circuit is connected, to avoid direct contact of an external probe tip on the detector's surface.

Data availability. The authors declare that all relevant data supporting the findings of this study are available within the paper and its Supplementary Information.